Supporting Information

Laser optothermal nanobomb for efficient flattening of nanobubbles in van der Waals materials

Jia-Tai Huang[1], Benfeng Bai[1,], Hong-Ren Chen[1], Peng-Yi Feng[1], Jian-Yu Zhang[1], Yu-Xiao Han[1], Xiao-Jie Wang[1], Hong-Wei Zhou[1], Yuan Chai[1], Yi Wang[1], Guan-Yao Huang[2], Hong-Bo Sun[1,*]*

[1] *State Key Laboratory of Precision Measurement Technology and Instruments, Department of Precision Instrument, Tsinghua University, Beijing 100084, China*

[2] *Key Laboratory for Thermal Science and Power Engineering of Ministry of Education, Beijing Key Laboratory of CO_2 Utilization and Reduction Technology, Department of Energy and Power Engineering, Tsinghua University, Beijing 100084, China.*

**Corresponding to: baibenfeng@tsinghua.edu.cn; hbsun@tsinghua.edu.cn*

1. Membrane model of nanobubbles in 2D materials

It is assumed that bubbles of different sizes at the MoS_2/SiO_2 interface can be described as the deflection of a pressurized membrane, which was described as[1, 2]

$$w(r)=h\left(1-\frac{r^2}{a^2}\right), \tag{1}$$

where h is center height, a is capping radii, and $w(r)$ is the deflection at a radial distance of r from the center.

The minimum energy value of the thin film substrate structure is reached at equilibrium, and the parameter relationship can be determined. The total energy Π of the system is calculated by:

$$\Pi=E_b^-+E_s^-+E_s^+ +\pi a^2\Delta\gamma-\Delta pV=2\pi\int_0^a U_b^-(r)rdr+2\pi\int_0^a U_s^-(r)rdr+$$
$$2\pi\int_0^a U_s^+(r)rdr+\pi a^2\Delta\gamma-\Delta pV, \tag{2}$$

where E_b^- reprents the bending energy of the film, E_s^- and E_s^+ are respectively the tensile energy inside and outside the nanobubble ($|r|\le a$, indicated by the superscript '-'; $|r|>a$, indicated by the superscript '+'); $\Delta\gamma$ is the adhesion energy per unit area and K is the in-plane elastic stiffness; Last term represents the free energy of the substance inside bubbles where Δp is the hydrostatic pressure. the energy per unit area corresponding to the first three physical quantities are U_b^-, U_s^- and U_s^+, whose specific expressions are respectively:

$$U_b^-(r)=\frac{D}{2}\left[\left(\frac{d^2w}{dr^2}\right)^2+\frac{1}{r^2}\left(\frac{dw}{dr}\right)^2+\frac{2v}{r}\frac{dw}{dr}\frac{d^2w}{dr^2}\right], \tag{3}$$

$$U_s(r)=\frac{K}{2\left(1-v^2\right)}\left(\varepsilon_r^2+2v\varepsilon_r\varepsilon_\theta+\varepsilon_\theta^2\right), \tag{4}$$

$$\Delta\gamma=\gamma_{fc}+\gamma_{fs}-\gamma_{sc}, \tag{5}$$

$$V=\frac{\pi}{2}ha^2, \tag{6}$$

where $D=Et^3/12(1-v^2)$ is the flexural rigidity of the film, in which E and v are the Young's modulus and Poisson ratio of the MoS_2 film; ε_r and ε_θ indicate the

radial and circumferential strains of the film (radial part indicated by the subscript 'r'; circumferential part indicated by the subscript 'θ'); $K = E_{in}t$ is the in-plane elastic stiffness, in which E_{in} and t are the in-plane Young's modulus and thickness. γ_{fc}, γ_{fs} and γ_{sc} represent the interfacial tensions between the film ('f'), the nanobubbles' content ('c'), and the substrate ('s'). For the 1L-MoS_2, the E, K, t and v is taken as 200 GPa, 120 N/m, 0.7 nm and 0.2, respectively according to the previous report.[3, 4]

It is assumed that the radial displacement by the Rayleigh-Ritz method:[5]

$$u^{-}(r) = u_0 \frac{r}{a}\left(1 - \frac{r^2}{a^2}\right) + u_s \frac{r}{a}, \tag{7}$$

where $u_s = u^{-}(a)$, and u_0 is a parameter to be determined. Considering that the shear interaction between the cap layer and the substrate may be weak, the sliding boundary condition is used. So the radial displacement outside the nanobubble is:

$$u^{+}(r) = u_s \frac{a}{r}. \tag{8}$$

From the displacement equation, the radial and circumferential strains inside and outside the nanobubble can be written as:

$$\begin{cases} \varepsilon_r^{-} = \dfrac{du^{-}}{dr} + \dfrac{1}{2}\left(\dfrac{dw}{dr}\right)^2 = \dfrac{u_0 + u_s}{a} - \dfrac{3u_0 r^2}{a^3} + \dfrac{2h^2 r^2}{a^4} \\ \varepsilon_\theta^{-} = \dfrac{u^{-}}{r} = \dfrac{u_0 + u_s}{a} - \dfrac{u_0 r^2}{a^3} \\ \varepsilon_r^{+} = -\varepsilon_\theta^{+} = -\dfrac{a u_s}{r^2} \end{cases}. \tag{9}$$

The radial stress between the edge of the nanobubble is continuous, and there are:

$$\varepsilon_r^{-} = \varepsilon_r^{+} \Rightarrow \frac{u_0 + u_s}{a} - \frac{3u_0 r^2}{a^3} + \frac{2h^2 r^2}{a^4} = -\frac{a u_s}{r^2} \Rightarrow u_s = u_0 - \frac{h^2}{a}. \tag{10}$$

According to Eq. (7) and (10), Eq. (9) can be written as with r:

$$\begin{cases} \varepsilon_r^- = \dfrac{1-v}{2}\dfrac{h^2}{a^2} + \dfrac{3v-1}{4}\dfrac{h^2 r^2}{a^4} \\ \varepsilon_\theta^- = \dfrac{1-v}{2}\dfrac{h^2}{a^2} + \dfrac{v-3}{4}\dfrac{h^2 r^2}{a^4} \\ \varepsilon_r^+ = -\varepsilon_\theta^+ = \dfrac{1+v}{4}\dfrac{h^2}{r^2} \end{cases}. \tag{11}$$

Further, according to Eq. (2)-(6) and Eq. (11). the key physical quantities can be obtained from variational arithmetic of the total energy Π:

$$\begin{cases} \left(\dfrac{\partial \Pi}{\partial u_0}\right)_a = 0 \Rightarrow u_0 = \dfrac{3-v}{4}\dfrac{h^2}{a} \\ \left(\dfrac{\partial \Pi}{\partial a}\right)_V = 0 \Rightarrow \Delta\gamma = 12(1+v)D\dfrac{h^2}{a^4} + \dfrac{5}{6}K\dfrac{h^4}{a^4} \\ \left(\dfrac{\partial \Pi}{\partial V}\right)_a = 0 \Rightarrow \Delta p = 16(1+v)D\dfrac{h}{a^4} + \dfrac{4}{3}K\dfrac{h^3}{a^4} \end{cases}. \tag{12}$$

For a pure membrane, the first D-related bending energy can be ignored. According to Eq. (12), the aspect ratio (h/a) can be obtained with $h/a \propto (\Delta\gamma/K)^{1/4}$. For gas-filled nanobubbles case, the $\Delta\gamma$ can be simply taken as the adhesion energy between the membrane and the substrate ($\Delta\gamma = \Gamma$). For the liquid-filled nanobubbles case, the interfaces between the liquid, the membrane and the substrate need to be considered, which can be written in the form below based on Young-Dupré equation:[6]

$$\Delta\gamma = \Gamma - \gamma_c\left(\cos\theta_f + \cos\theta_s\right), \tag{13}$$

where Γ represents the adhesion energy of the membrane substrate interface; γ_c is the surface tension of the contents, and the value of water is around 0.078 J/m^2; the water contact angle of the membrane and substrate are respectively θ_f and θ_s. Therefore, the aspect ratio of the liquid-filled nanobubble can be determined as the formula below with a small value compared to the gas-filled one:

$$\frac{h}{a} = \left(\phi\frac{\Gamma - \gamma_c\left(\cos\theta_f + \cos\theta_s\right)}{K}\right)^{1/4}, \tag{14}$$

where ϕ is a dimensionless coefficient, which is related to the shear properties of the vacuole edge.[3]

2. Details of simulation of temperature under laser irradiation

The finite-element method (FEM) with the heat transfer module of the COMSOL Multiphysics 5.6 was used to simulate the temperature distribution of the sample under laser irradiation. With a two-dimensional axisymmetric symmetry model, the configuration consisted of a 20 μm-thick SiO_2 substrate and a 0.7 nm thick MoS_2 layer with a width of 30 μm in geometry. We used the physical properties of SiO_2 included in the material library, for MoS_2, we assumed the values 103 W m^{-1} K^{-1}, 5.06 g cm^{-3}, 380 J kg^{-1} K^{-1} for the thermal conductivity,[7] density,[8] and specific heat capacity,[9] respectively.

For the physics conditions, the 'Heat Transfer in Solids' model was used in the simulation. The laser played the role of heat source in Gaussian functions, which was simulated by setting the heat source with the form below:

$$Q=\frac{P_H\alpha}{t\pi r_H^2}\exp(-\frac{r^2}{r_H^2})+\frac{P_L\alpha}{t\pi r_L^2}\exp(-\frac{r^2}{r_L^2}), \tag{15}$$

where α = 0.1 is the absorbance of the 1L-MoS_2 film and the SiO_2 at 532 nm wavelength, t = 0.7 nm is the thickness of the 1L-MoS_2 film. For the single-shot LOTB case, the puncture-beam with the power P_H = 7.5 mW and radius r_H = 0.15 μm while the power of the flattening-beam was set as P_L = 0 mW (no flattening-beam); For the dual-beam cascaded LOTB, the puncture-beam with the same power and radius, the flattening-beam with the P_L = 25 mW and radius r_L = 2.5 μm. The temperature at the bottom of the SiO_2 domain and outer range of SiO_2 and sample was fixed at the ambient temperature (300 K).

3. Stress analysis and characterization in nanobubbles under irradiation

In addition to the phase transition, the stress-pulling effect from the expansion of nanobubbles under laser irradiation could help flatten the 1L-MoS_2. The stress at any point of the nanobubble can be obtained by the constitutive relation of the MoS_2 film. Acording to Eq. (11) and (12), the radial and circumferential tensile forces corresponding to the unit length can be calculated in weak shear limit:[10]

$$\begin{cases} N_r^- = \sigma_r^- t = \dfrac{K}{1-v^2}\left(\varepsilon_r^- + v\varepsilon_\theta^-\right) = K(\dfrac{1}{2}\dfrac{h^2}{a^2} - \dfrac{1}{4}\dfrac{h^2 r^2}{a^4}) \\ N_\theta^- = \sigma_\theta^- t = \dfrac{K}{1-v^2}\left(\varepsilon_\theta^- + v\varepsilon_r^-\right) = K(\dfrac{1}{2}\dfrac{h^2}{a^2} - \dfrac{3}{4}\dfrac{h^2 r^2}{a^4}) \\ N_r^+ = -N_\theta^+ = \dfrac{K}{1-v^2}(1-v)\varepsilon_r^+ = \dfrac{K}{4}\dfrac{h^2}{r^2} \end{cases}. \quad (16)$$

The outside stress N_r^+ decays with the square of the distance in space. For the nanobubble with a radius equal to 200 nm, it expands with the aspect ratio increasing from 0.04 to 0.07 under laser irradiation (according to the experiment in Fig. 1b). The distribution of the increased tensile $\Delta N_r^+ = N_r^+\Big|^{h/a=0.07} - N_r^+\Big|^{h/a=0.04}$ is calculated by Eq. (16) and plotted in Fig. S1a, which shows increased tensile stress in the order of 0.1 N/m could be generated around the single nanobubble under laser irradiation.

Since the position of Raman peaks reflects the strain situation of the 1L-TMDs and the $E_{2g}{}^1$ and A_{1g} peaks of 1L-MoS_2 will red shifts under strain,[11, 12] detailed Raman studies were carried out to experimentally confirm the enhancement of strain and stress on expanded nanobubble under laser irradiation. However, the temperature rise under laser irradiation may also cause a red shift in the Raman peak (-0.013 cm^{-1}/K and -0.016 cm^{-1}/K for $E_{2g}{}^1$ peak and A_{1g} peak) according to previous report.[11]

Since only the nanobubbles area exists the increased tensile stress under laser irradiation, to rule out the influence of the temperature increase, as shown in Fig. 1e, we measured Raman spectra from the nanobubble area (solid curves) and nearby flat area (dashed curves) on a 1L-MoS_2 film under high-power (2 mW, red curves) and low-power (0.2 mW, blue curves) irradiation lasers. The changes in strain of the sample are negligible with low-power. At the flat area, the shift in Raman peaks is only due to the

temperature rise; At the nanobubble area, the shift in Raman peaks is due to both the temperature rise and strain increase. Since the temperature rise of the flat and nanobubble is similar, the part of the strain at the nanobubble area can be determined by subtracting the peak shift in the flat area. As shown in the inset of Fig. S1b, for the flat area, the two peaks have a red shift of 2 cm^{-1} (397 cm^{-1} to 395 cm^{-1} for E_{2g}^1, 414 cm^{-1} to 412 cm^{-1} for A_{1g}), while for the nanobubble area, the E_{2g}^1 and A_{1g} peaks have a red shift of 4 cm^{-1} and 3 cm^{-1} (396 cm^{-1} to 392 cm^{-1} for E_{2g}^1, 414 cm^{-1} to 411 cm^{-1} for A_{1g}), respectively. The extra Raman red shift on the nanobubble area ($\Delta E_{2g}^1 = 2$ cm^{-1}, $\Delta A_{1g} = 1$ cm^{-1}) can be attributed to the change in strain. According to previous reports,[23] the ratio of the E_{2g}^1 shift concerning strain is about 3.2 cm^{-1}/% in CVD-grown 1L-MoS_2,[13] which calculates the increasing strain equals around 0.63% in this nanobubble by dividing the extra shift of E_{2g}^1 by this ratio.

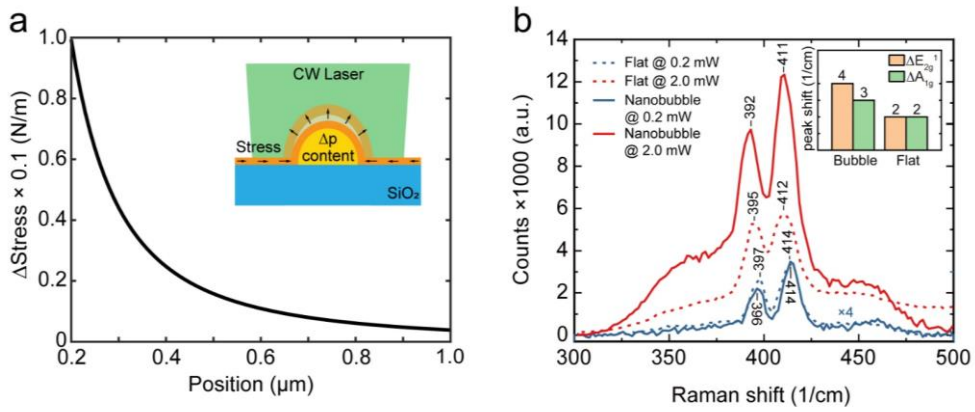

Figure S1. Stress analysis and characterization in nanobubbles under laser irradiation. (a) Calculated stress distribution around a nanobubble of radius 200 nm. The inset schematically illustrates the nanobubble expansion and exerted tensile stress distribution under laser irradiation. (b) Measured Raman spectra from the nanobubble area (solid curves) and nearby flat area (dashed curves) on a 1L-MoS_2 film under high-power (red curves) and low-power (blue curves) irradiation lasers. The inset shows the spectral shifts of two Raman peaks in the nanobubble area and flat area.

4. Change of pressure and aspect ratio inside nanobubbles with temperature

Considering the gas-filled nanobubble, ignoring the first D-related bending energy in Eq. (12), the relation between the temperature and the aspect ratio of the nanobubble can be written in the form below according to the ideal gas law $pV = nRT$:

$$\frac{\pi p_0 a^3}{2}\frac{h}{a} + \frac{2\pi K a^2}{3}\left(\frac{h}{a}\right)^4 = nRT, \tag{17}$$

Where the in-plane elastic stiffness K =120 N/m for monolayer MoS_2. Take aspect ratio equals 0.06 when temperature equals 373 K according to the experimental results in Fig. 1d, the relation curve of the aspect versus temperature can be obtained as shown in Figure below. It shows that when increasing the temperature, the gas-filled nanobubble keeps expanding with the aspect ratio nearly linear increasing, and the aspect ratio expands to 0.074 when the temperature is close to the sublimation temperature of the monolayer MoS_2 (723 K). The result not only confirms that the content inside the nanobubble is liquid initially by comparing the experiment results with the mutation curve in Fig. 1d (if the content inside the nanobubble is gas initially, the experiment results should be nearly linear curve as Fig. S2), but also provides a method to characterize the temperature of the nanobubbles.

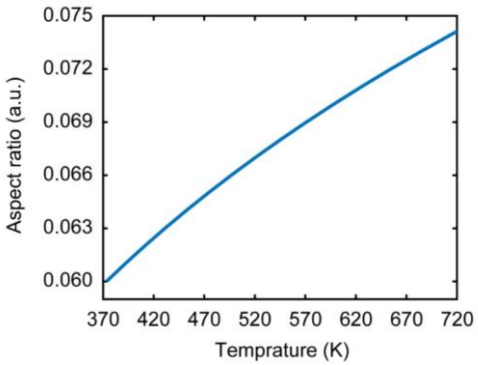

Figure S2. Simulated change of aspect ratio with temperature

5. Optical image of the 1L-MoS_2 sample

As the optical image shown in Fig. S3, the samples used in this research were 1L-MoS_2 flakes grown via the CVD method and distributed all around the substrate, each flake exhibiting a triangular shape with side lengths ranging from 10 to 30 μm.

Figure S3. Optical image of 1L-MoS_2 sample

6. Analysis of the nanobubbles' composition

The inclusion of nanobubbles in 2D materials (gas- or liquid-filled) can be identified based on at least the following three aspects:

1. According to the pressurized membrane model of 1L-MoS_2, the gas-filled nanobubbles have a higher aspect ratio compared to the liquid-filled nanobubbles.[14] And the aspect ratio of nanobubbles on our sample (as small as ~0.04) is similar to the case of the liquid-filled blister with the material system of MoS_2/SiO_2 reported before.[3]
2. Gas- and liquid-filled nanobubbles exhibit distinct trends in aspect ratio variation as the temperature increases. According to the simulation result the aspect ratio is nearly proportional to the temperature in gas-filled nanobubbles, however, as the result of the aspect ratio under different irradiation laser power shown in Fig. 1d, the aspect ratio of the nanobubbles in our sample exhibit an abrupt change when reached the temperature threshold, which is characteristic of liquid inclusion inside the nanobubbles.
3. The gsa-filled nanobubbles could fully deflate within hours or days according to the previous report.[3] And the nanobubbles on our sample remain > 2 years.

Based on the above three analyses, it can be concluded that the nanobubbles formed during the wet-transfer process we used are liquid-filled. In fact, the experiments

conducted in measuring the aspect ratio change of a nanobubble under different irradiation laser power (Fig. 1d, aspect 2 mentioned above) offer a novel approach for distinguishing between liquid- and gas-filled nanobubbles through the combination of optical and mechanical methods.

Besides, since the transfer process is conducted in a deionized water environment and the PMMA is removed by immersing in acetone 3 ~ 5 times, each for 30 minutes, the nanobubbles' inclusion is expected to be predominantly composed of water. According to the previous literature on spectroscopic analysis of the nanobubbles' inclusion,[15] we have carried out the additional nanoscale Fourier transform infrared spectroscopy (Nano-FTIR) experiment to confirm if the organic residues are present. The Nano-FTIR was conducted using the commercial system (Nano-FTIR, neaspec), which combines s-SNOM equipped with broadband illumination and FTIR-based detection developed by neaspec. It provides FTIR spectroscopy at the spatial resolution of AFM, delivering nanoscale chemical identification and hyperspectral imaging. As the spectrum shown in Fig. S4 up, which illustrates the nano-FTIR results of the substrate (red line), flat region of 1L-MoS_2 (blue line) and nanobubble region (green line), the three crosses in the inset marked the measurement position. And no obvious peak in PMMA absorption peak (1726 cm^{-1}) was observed. To further confirm this problem, we have carried out the line scan of nano-FTIR across a single nanobubble. As shown in Fig. S4 down below, the blue line in Fig. S4 down dictates the topography curve of the nanobubble, and the red line indicates the intensity of the nano-FTIR absorption at 1725 cm^{-1}. The spatial step was 20 nm. The curve shows that there is no obvious change in the nano-FTIR intensity at the nanobubble. The results indicate the inclusion of nanobubbles do not present a considerable amount of organic compounds such as PMMA.

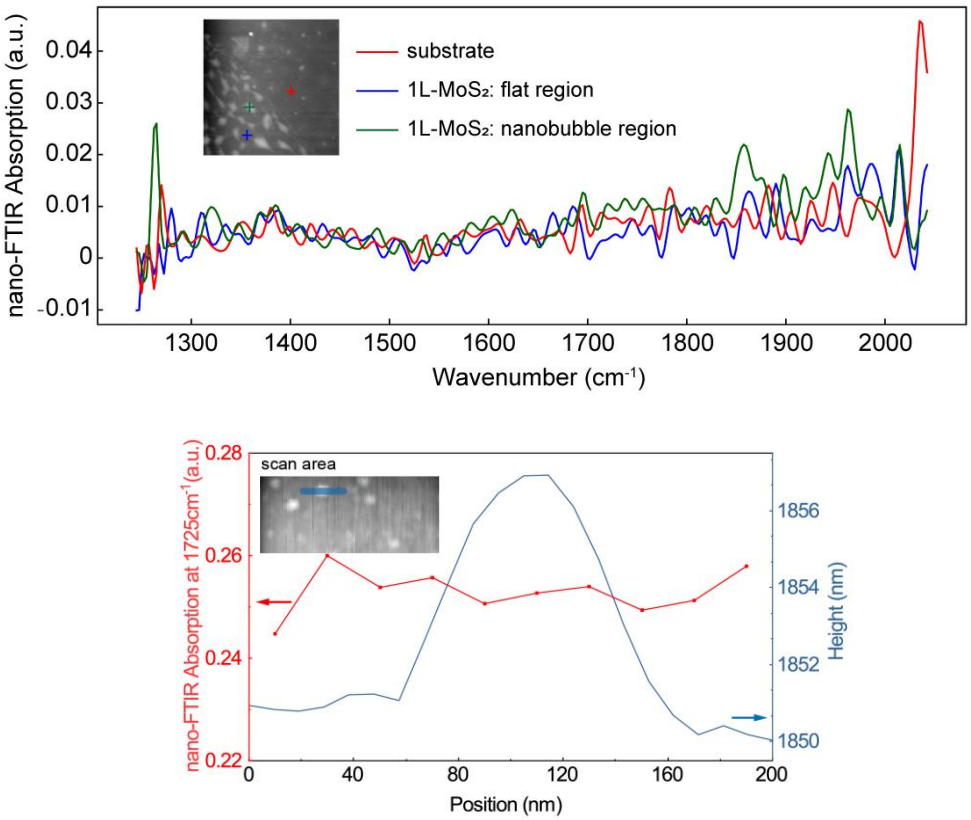

Figure S4. (up) Nano-FTIR characterization of 1L-MoS_2 sample; (down) Nano-FTIR line mapping of 1L-MoS_2 nanobubble at 1725 cm^{-1}.

7. Absorption spectrum of 1L-MoS_2 sample and the selection of excitation source

The wavelength of the excitation source was selected to correspond to the side absorption band of 1L-MoS_2 so that the temperature field can be formed and the film can sublime to create a void. To confirm this problem, we have experimented to measure the absorption spectrum of 1L-MoS_2 on SiO_2. The microscale absorption spectrum of the sample was obtained by a spectrometer (DU970P-BVF, Andor) combined with a confocal microscope (A1, Nikon).

As shown in Fig. S5, 1L-MoS_2 is a direct bandgap semiconductor, exhibiting edge band absorption properties, which can absorb photons with energies above their optical bandgap (as the absorption edge ~650 nm). The two absorption peaks correspond to the A exciton (peak at 646.5 nm) and B exciton (peak at 599.1 nm) of 1L-MoS_2 respectively. As the green dashed line indicated in Fig. S5, the selection of our laser source

corresponds to the absorption range of 1L-MoS_2, allowing the laser energy to be efficiently absorbed by the material, thereby generating the corresponding temperature field distribution.

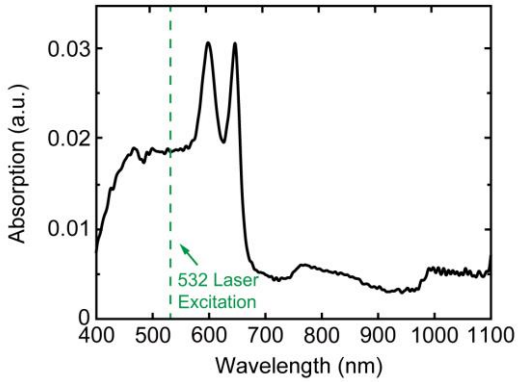

Figure S5. Absorption spectrum of the 1L-MoS_2 sample, the green dashed line indicates the selected 532 nm excitation laser.

8. Error analysis

To confirm the measurement error during topography mapping, the stability experiment of AFM by measuring one point with the probe frozen was carried out. As shown in Fig. S6, the height at a single point exhibits drift over time, which determines the RMS of height as $RMS_h = 0.01$ nm. Assuming the measurement errors in height follow a Gaussian distribution, approximately 95% of the data fall within the range of $\pm 2RMS_h$. Therefore, the height uncertainty can be considered as $\sigma_h = 2RMS_h = 0.02$ nm. And the mapping step is set as 10 nm during the topography mapping, so that the radius uncertainty can be considered as $\sigma_a = 10$ nm.

Considering the error propagation formula, the uncertainty of the aspect ratio σ_R can be expressed as:

$$\begin{aligned}\sigma_R^2 &= (\frac{\partial R}{\partial h})^2 \sigma_h^2 + (\frac{\partial R}{\partial a})^2 \sigma_a^2 \\ &= (\frac{1}{a})^2 \sigma_h^2 + (\frac{h}{a^2})^2 \sigma_a^2\end{aligned} . \tag{18}$$

For a nanobubble with a height of 8 nm and radius of 200 nm (the aspect ratio equal to 0.04), the uncertainty of the aspect ratio can be determined as 0.002 (relative uncertainty ~5%).

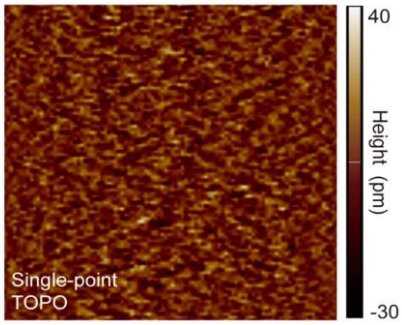

Figure S6. Single-point height measurement

9. Analysis of the formed wrinkle after LOTB

The wrinkles are residual structures[1] mainly formed by the directional movement and convergence of nanobubbles' inclusion under laser irradiation.

The directional movement of nanobubbles' inclusion can be analyzed by the stress distribution of the film. As shown in Fig. S7, a nanobubbles around the laser irradiation site is subjected to four different stresses at the boundary, and the stress effects are categorized into two parts based on the film peeling model as: (i) Prevent delamination: including adhesion force (film-substrate) and capillary force (aqueous layer); (ii) Promote delamination: including bending stress (film) and pressure gradient stress. As the stress varies over time and space, the film is continuously delaminated and re-adhered to the substrate, allowing the inclusion to be transferred out of the interlayer gaps.[16]

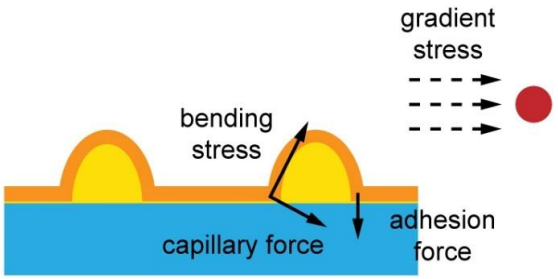

Figure S7. The schematic diagram of the force analysis of nanobubbles.

The inclusion with directional transfer is more likely to converge with surrounding nanobubbles' inclusion to form a larger structure, such as wrinkle, when they are unable to flow out and remain in the interlayer. This can be quantified by using the isolated bubble energy model[17] expressed as a function of the number of gas molecules (N):

$$\begin{aligned} F(N) &= \Pi(N) + \pi a^2 \Delta\gamma \\ &= \frac{3NkT}{2}\left\{1 - \frac{1}{3}\ln\left[NkT\left(\frac{\phi(v)p_0^4}{K\Gamma^5}\right)^{1/2}\right]\right\}. \end{aligned} \tag{19}$$

Where k is Boltzmann constant, T is temperature, Γ is adhesion energy of the film-substrate interface, and $\phi(v)$ is a constant related to Poisson's ratio. For two nanobubbles with the number of gas molecules N_1 and N_2, respectively, the inequality $F(N_1+N_2) < F(N_1)+F(N_2)$ shows the tendency of nanobubbles to exhibit spontaneous minimization of energy through convergence.

Therefore, due to the directional movement driven by the differential pressure and the convergence effect for energy reduction, wrinkles form in regions where the cumulative strain energy is lower than the interfacial adhesion energy, independent of the initial strain distribution even in flattened area.[17]

In practice, considering the laser irradiation site, original spatial distribution of adjacent nanobubbles and spatial heterogeneity of the adhesion, the formation of wrinkles exhibits a certain degree of randomness. In practice, the flattening effect of the LOTB is mainly influenced by the location of laser irradiation and the original spatial distribution of adjacent nanobubbles, and the formation of wrinkles exhibits a certain degree of randomness. As shown in Fig. S8 below, the nanobubbles were eliminated with no wrinkles remaining after the single-shot LOTB treatment (laser power equals 7.5 mW). On the other hand, as the multi-shot LOTB results shown in Fig. 4, the introduction of multi-beam irradiation can effectively reduce wrinkle residues after LOTB treatment.

10. Effect of LOTB in different irradiation regions

In practice, the flattening effect of the LOTB is mainly influenced by the location of laser irradiation and the original spatial distribution of adjacent nanobubbles, which makes it difficult to accurately statistically quantify the treatment effects across regions due to the random distribution of initial nanobubbles. To confirm the reproducibility of the LOTB method, in addition to the result in Fig. 2, three representative cases of LOTB effects observed across different samples and regions are shown in Fig. S8. For flake 1 in Fig. S8a, d, g (the first column), the laser irradiates the area distant from the nanobubbles, and the flattening effect was observed with numerous nanobubbles distant from the irradiation center being effectively eliminated. As shown in Fig. S8g, the height RMS and SAR decrease by 71% (3.1 nm to 0.9 nm) and 78% (0.14% to 0.03%) after irradiation. For flake 2 in Fig. S8b, e, h (the second column), the laser irradiates the area close to the nanobubbles, and the flattening effect was more obvious with most nanobubbles being effectively eliminated. As a result shown in Fig. S8h, the height RMS and SAR decreased by 77% (2.6 nm to 0.6 nm) and 82% (0.11% to 0.02%) after irradiation. The results from flakes 1 and 2 demonstrate the reproducibility of the LOTB method both when the irradiation site is close to and distant from nanobubbles. Notably, better flattening is observed when the laser spot is located near nanobubbles, primarily due to the increased number of nanobubbles within the effective interaction range.

Besides, for flake 3 in Fig. S8c, f, i (the third column), an impurity was present in the area of laser irradiation, in this case, the flattening effect of the LOTB method remains, though its efficiency is slightly reduced with height RMS and SAR decrease by 30% (1.7 nm to 1.2 nm) and 50% (0.16% to 0.08%) after irradiation, which may due to the impurity affecting the absorption of optical energy in the film. The results, including the results in Fig. 2 (height RMS and SAR decrease by 71% and 79%), demonstrate the reproducibility of the LOTB method even when irradiating on impurity, and when the laser energy is fully absorbed by the film, the flattened effect consistently exceeds 70% in both height RMS and SAR.

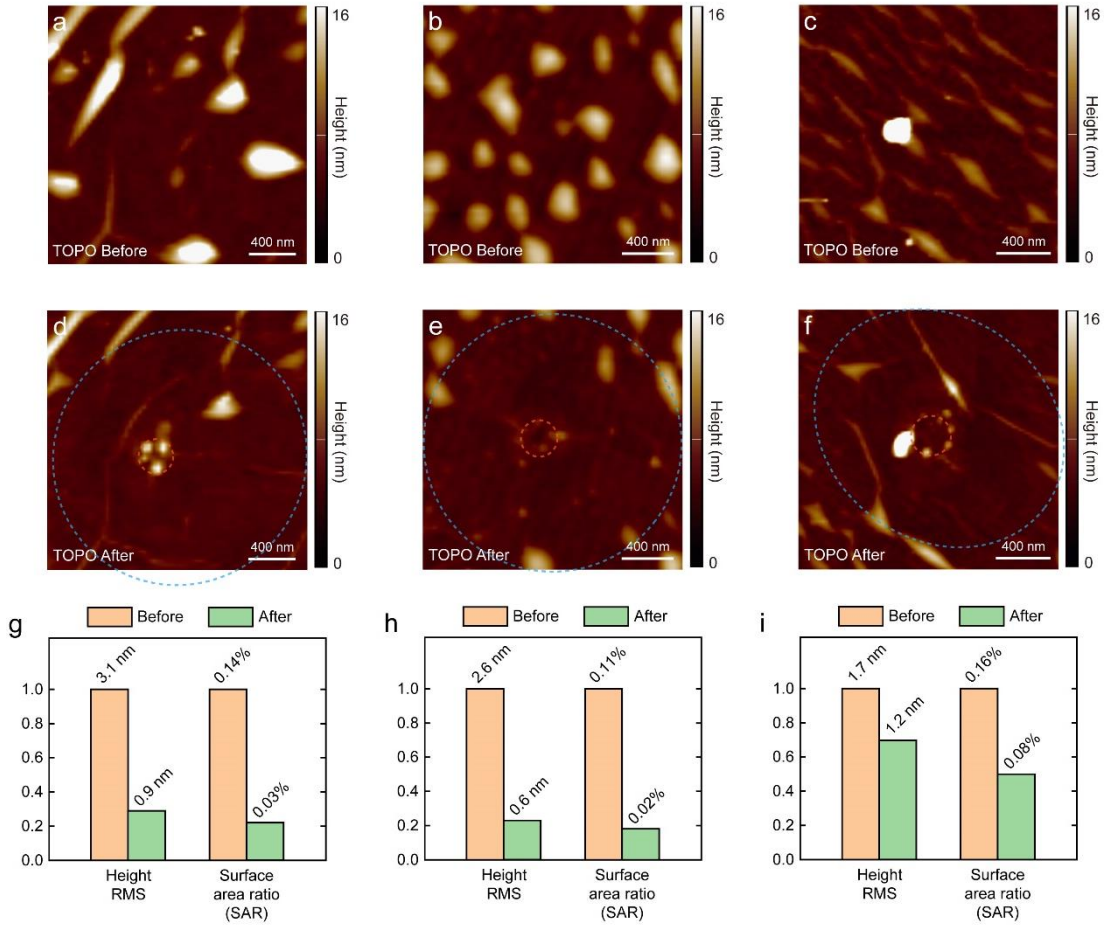

Figure S8. Effect of single-shot LOTB in different flakes and irradiation regions. (a)-(c) The topography before and (d)-(f) after single-shot LOTB. (g)-(i) Surface roughness statistics of the flattened region before and after LOTB. Three flakes with the irradiation site distant from (first column), close to (second column) nanobubbles, and on an impurity (third column).

11. Effect of LOTB on hBN substrate

In principle, the thermal conductivity and adhesion energy of different substrates can influence the temperature distribution under optical irradiation, as well as the aspect ratio of the nanobubbles, as derived in SI that the aspect ratio $h/a \propto (\Delta\gamma/K)^{1/4}$. However, these factors primarily affect the laser parameters required (e.g., substrates with higher thermal conductivity may require higher power to achieve the same thermal

field, and the temperature field has a smaller gradient) but do not compromise the effectiveness of the LOTB mechanism.

To experimentally confirm the applicability of this technology to other substrates, we have carried out additional experiments on the sample with hBN substrate, which is the most common substrate used in 2D materials devices for the atomically flat surface and dielectric screening effect. The hBN substrate was grown and prepared, and then the 1L-MoS_2 was also transferred to the hBN substrate with a thickness of 10 nm through the same KOH-based wet transfer method used before (see details in Methods). The growth and transfer are both performed by 6Carbon Technology (Shenzhen). It is worth noting that since h-BN is also a layered material, nanobubbles may also form during the preparation. The nanobubbles originating from MoS_2 and hBN can be distinguished by their aspect ratios, as h-BN exhibits stronger adhesion energy, resulting in larger aspect ratios.[18]

Similar to Fig.2, the single shot LOTB was performed to treat the 1L-MoS_2 with hBN substrate, the laser power equals 8.5 mW. As the topography before and after laser irradiation shown in Fig. S9, a similar surface flattening effect was also observed around the center of irradiation, which proves the applicability of the LOTB method in different substrate. The remaining nanobubbles with larger aspect ratios may originate from the h-BN substrate itself, which can further be eliminated by adjusting the laser wavelength and power.

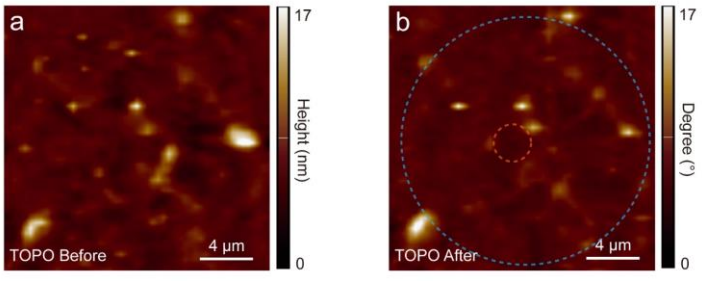

Figure S9. Effect of the single-shot LOTB in 1L-MoS_2 with hBN substrate

12. Effect of single-shot LOTB with lower power

The selection of laser power is critical and requires careful optimization.

Insufficient power fails to induce a stable phase transition effect, whereas excessive power leads to extensive material ablation. According to the FEM simulation (shown in Fig. 1b) and experiments, the 7.5 mW is a suitable power to induce the LOTB effect without causing significant material ablation of 1L-MoS_2. The LOTB result of lower power (4 mW) was illustrated in Fig. S10 below, it was observed that the lower laser irradiation led to the elimination of nanobubbles within a localized central region; however, no significant flattening effect was detected over a broader area compared to the result in Figure 2d (7.5 mW).

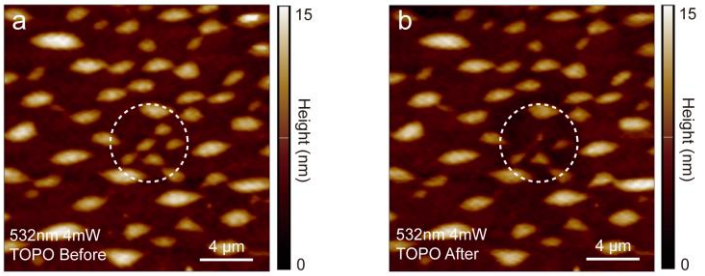

Figure S10. Topography of 1L-MoS_2 with nanobubbles (a) before and (b) after laser modification with a lower power of 4 mW.

13. AFM phase mapping of treated sample under single-shot LOTB

AFM phase is one of the commonly used mechanical characterization technologies to map variations in surface properties, which can be generated in addition to the topography image when the AFM is operated in tapping mode. It depends on the interaction between the tip and surface, including the properties of the surface, such as adhesive, stiffness or frictional properties, the interaction between the tip and surface will cause the oscillation to lag (i.e., a phase shift).[19] And the change of AFM phase at the irradiation region may come from the weak absorption of heat by the SiO2 substrate. Therefore, the selection of excitation source wavelength should correspond to the absorption band of the sample. As shown in Fig. S11b, the AFM phase of the flattened region was obviously even after laser modification with the spatial inhomogeneity reduced by 60.8% in RMS, which also indicates the mechanical properties of the film

at the original nanobubbles location have not changed after flattening through laser modification. Besides, there is a decrease in the AFM phase around the sacrifice region, which could be due to the laser-oxidation effect in the region with a temperature above 250 ℃.[20]

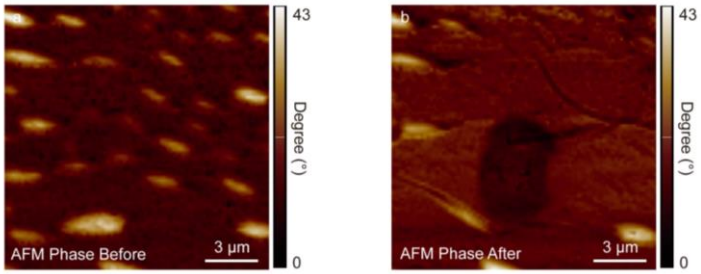

Figure S11. AFM phase of 1L-MoS_2 with nanobubbles (a) before and (b) after sing-shot LOTB modification.

14. Effect of LOTB with near-infrared laser

As a comparison, we have carried out the additional LOTB experiment with the near-infrared laser, which is outside the absorption band of 1L-MoS_2, so the energy is difficult to be absorbed by the material, making it difficult to establish a temperature gradient field. In detail, the 780 nm laser (ErFemto-780MP, ROI) with a repetition rate of 80 MHz was used to illustrate the same sample for comparison. As the result shown in Figure R12 below, the power set up to 20 mW, there is no obvious flattening effect in topography (Fig. S12a) at the irradiation region (marked as the white dashed circle) with the 780 nm laser, and the change of AFM phase at the irradiation region may come from the weak absorption of heat by the SiO_2 substrate. Therefore, the selection of excitation source wavelength should correspond to the absorption band of the sample.

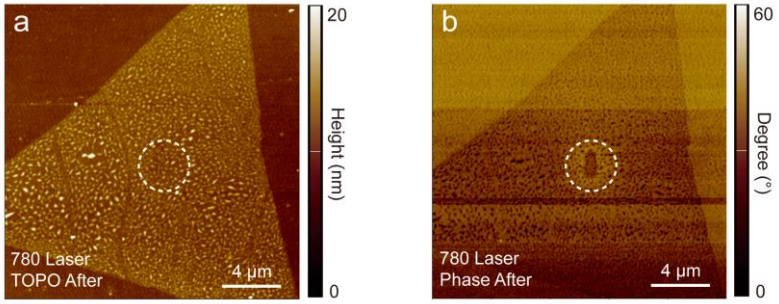

Figure S12. (a) Topography and (b) AFM phase of 1L-MoS_2 with nanobubbles after laser modification with 780 nm laser. The white dashed cycles indicate the irradiation points.

15. Time scale of LOTB treatment

To confirm the time scale of the LOTB method, we have carried out the experiments with different treated times under the same power (6 mW) by controlling the duty ratio through the TTL (transistor-transistor logic) modulation of the CW laser source. As shown in Fig. S13, nearly no effect when the treatment time is too short (as the result of 10 ms in the left), the effect of nanobubbles elimination begins to appear at 20 ms with the nanobubbles's inclusion tending to gather in the middle, and the effect becomes obvious after 50 ms. The result indicates the time scale of LOTB can be determined as around 50 ms.

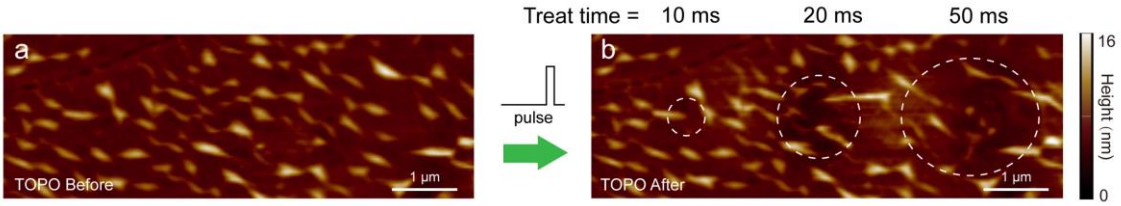

Figure S13. AFM Topography of 1L-MoS_2 with nanobubbles (a) before and (b) after LOTB with different treat times.

The irradiation time should be larger than the time required for the thermal field to become fully established; thus, longer irradiation times are generally more favorable. On the other hand, the time-dependent experiment indicates that the time scale of LOTB can be determined as around tens of milliseconds, thus it is suggested that the minimum effective irradiation time should be larger than 50 ms. In fact, the experimental results in the manuscript were obtained using a laser irradiation time of ~1 s.

16. Effect of LOTB with ps laser

To confirm the heat effect and rule out the field effect and shock wave by laser during the LOTB modification, we have carried out a similar experiment using the single ps laser. The 1030 nm laser with a pulse width of 4 ps (FemtoYL-20, OYSL) was converted into 515 nm through a BBO (beta-BaB_2O_4) second-harmonic crystal and irradiated onto the sample through the oil-immersed objective. As shown in Fig. S14b, the white dashed cycles indicate the irradiation points, and the single pulse energy of each column from top to bottom is 5.6 nj, 8.6 nj, and 57.8 nj respectively. With ultra-high transient power, the sample on irradiation point ablation soon, however, the surrounding sample doesn't change through topography characterization. The results of ps laser rule out the ultra-fast interaction effect and confirm that it's the laser heating effect dominates the LOTB method.

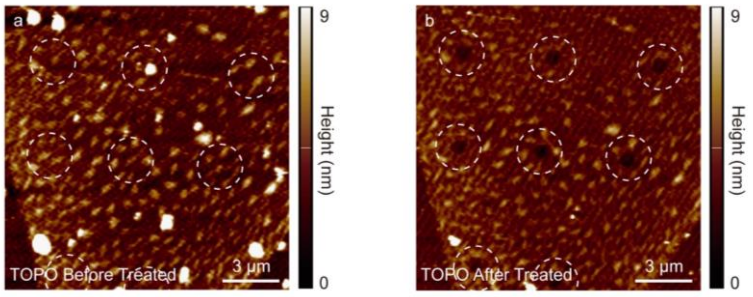

Figure S14. Topography of 1L-MoS_2 with nanobubbles (a) before and (b) after laser modification with ps laser (4ps @515 nm). The white dashed cycles indicate the irradiation points.

17. Long-term stability of the LOTB-treated regions

To evaluate the long-term stability of the LOTB-treated regions, we performed a repeated AFM topographic mapping on the same area in Fig. 2d after 13 months. During this period, the surrounding relative humidity fluctuated from approximately 5% to 80%, and the temperature fluctuated from approximately 10°C to 30°C. The AFM image obtained after 13 months is presented in Fig. S15 below, where rectangular marks left by the previous scan can still be clearly observed. Notably, the topography of the

flattened region remains nearly unchanged, with no effect of new nanobubble formation. This proves that the LOTB treatment exhibits excellent long-term stability with no reformation of nanobubbles even under large changes in temperature and humidity over extended periods.

On the other hand, nanoparticles appeared in the central sacrifice region, exhibiting a high aspect ratio of up to ~0.14, which is significantly greater than that of typical nanobubbles (~0.04). These particles are likely impurities or molybdenum oxide, possibly formed from incomplete sublimation of Mo (since the chalcogen elements exhibit higher chemical reactivity) followed by reactions with atmospheric O_2 and H_2O.[21] However, since these particles are confined to the sacrifice region, they do not affect the properties of the flattened region. Furthermore, such nanoparticles could potentially be avoided by employing higher-power laser irradiation to ensure complete sublimation of Mo atoms.

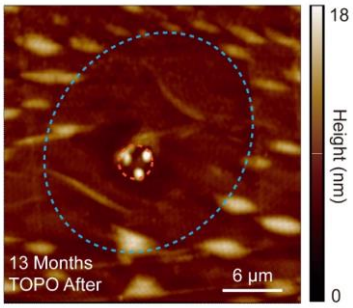

Figure S15. Topography of the same area in Fig.2d after 13 months

18. Dual-beam cascaded LOTB setup

The setup combining the modules of laser modification and signal detecting is shown in Fig. S16a. Two lasers are introduced to the microscope, one is collimated with the same focal plane as the microscope, and the other one is divergent through a lens (f = 1000 mm) so that the spot is much larger at the focal plane of the microscope. As shown in Figs. S6b-c, the spot of the puncture-beam with a small diameter close to 0.3 μm the diffraction limit, while the spot of the flattening-beam with a large diameter close to 5 μm, which is controlled by the focal length and position of the lens.

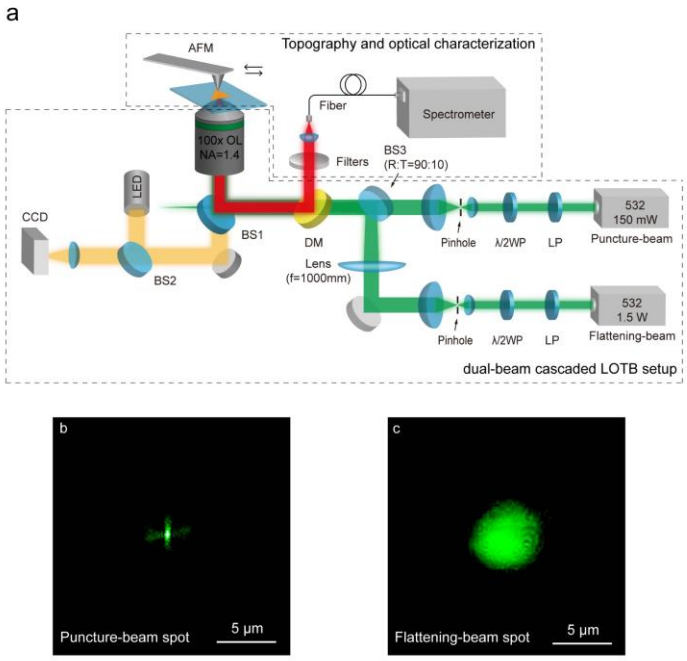

Figure S16. (a) Instrumental setup of LOTB system with deal-beam cascaded. The spot image of the (b) puncture-beam and (c) flattening-beam obtained by the camera.

19. AFM phase mapping of sample treated with dual-beam cascaded LOTB

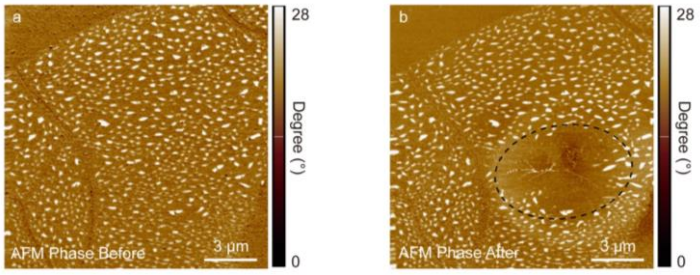

Figure S17. AFM phase of 1L-MoS_2 with nanobubbles (a) before and (b) after dual-beam cascaded LOTB modification.

20. Effect of dual-beam cascaded LOTB without the puncture-beam

To confirm the mechanism of the dual-beam cascaded LOTB method, the experiment with only the flattening-beam was conducted. The power of the flattening-beam was 25 mW same as before and the power of the puncture-beam was zero. As the irradiated region (white dashed line) is shown in Fig. S18, the flattened region shows no obvious change. This can be explained by the fact that without the Focused laser,

there is no normal channel with pressure difference to enable the content inside nanobubbles to escape.

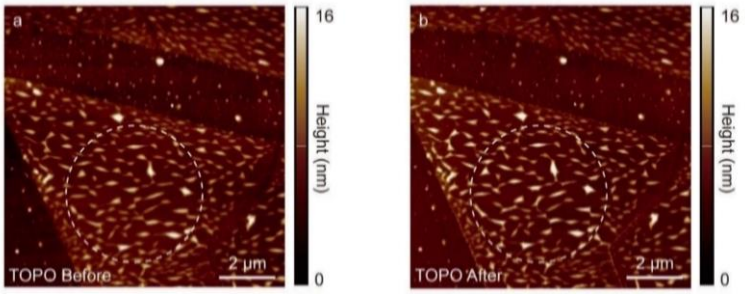

Figure S18. Topography of 1L-MoS_2 with nanobubbles (a) before and (b) after LOTB modification with only the flattening-beam. The white dashed cycles indicate the irradiation area.

Reference:

1. Ma, C., Chen, Y. & Chu, J. Time-Dependent Pinning of Nanoblisters Confined by Two-Dimensional Sheets. Part 1: Scaling Law and Hydrostatic Pressure. *Langmuir* **39**, 701-708 (2023).
2. Jiang, J.-W., Park, H.S. & Rabczuk, T. Molecular dynamics simulations of single-layer molybdenum disulphide (MoS_2): Stillinger-Weber parametrization, mechanical properties, and thermal conductivity. *Journal of Applied Physics* **114**, 064307 (2013).
3. Sanchez, D.A. et al. Mechanics of spontaneously formed nanoblisters trapped by transferred 2D crystals. *Proceedings of the National Academy of Sciences* **115**, 7884-7889 (2018).
4. Hung, N.T., Nugraha, A.R.T. & Saito, R. Two-dimensional MoS_2 electromechanical actuators. *Journal of Physics D: Applied Physics* **51**, 075306 (2018).
5. Lurie, A.I. Theory of elasticity (Springer Science & Business Media, 2010).
6. Rafiee, J. et al. Wetting transparency of graphene. *Nature Materials* **11**, 217-222 (2012).
7. Peng, B. et al. Thermal conductivity of monolayer MoS_2, $MoSe_2$, and WS_2: interplay of mass effect, interatomic bonding and anharmonicity. *RSC Advances* **6**, 5767-5773 (2016).
8. Su, J. et al. Effect of temperature on thermal properties of monolayer MoS_2 sheet. *Journal of Alloys and Compounds* **622**, 777-782 (2015).
9. Cai, Y. et al. Lattice vibrational modes and phonon thermal conductivity of monolayer MoS_2. *Physical Review B* **89**, 035438 (2014).
10. Chernikov, A. et al. Exciton binding energy and nonhydrogenic Rydberg series in monolayer WS_2. *Physical Review Letters* **113**, 076802 (2014).
11. Lanzillo, N.A. et al. Temperature-dependent phonon shifts in monolayer MoS_2. *Applied Physics Letters* **103** (2013).

12. Castellanos-Gomez, A. et al. Local Strain Engineering in Atomically Thin MoS_2. *Nano Letters* **13**, 5361-5366 (2013).
13. Li, Z. et al. Efficient strain modulation of 2D materials via polymer encapsulation. *Nature Communications* **11**, 1151 (2020).
14. Khestanova, E. et al. Universal shape and pressure inside bubbles appearing in van der Waals heterostructures. *Nature Communications* **7**, 12587 (2016).
15. Sanchez, D.A., Dai, Z. & Lu, N. 2D Material Bubbles: Fabrication, Characterization, and Applications. *Trends in Chemistry* **3**, 204-217 (2021).
16. Wang, E. et al. Water nanolayer facilitated solitary-wave-like blisters in MoS2 thin films. *Nature Communications* **14**, 4324 (2023).
17. Jiang, J.-W., Park, H.S. & Rabczuk, T. Molecular dynamics simulations of single-layer molybdenum disulphide (MoS2): Stillinger-Weber parametrization, mechanical properties, and thermal conductivity. *Journal of Applied Physics* **114** (2013).
18. Bi, J. et al. Flat-top beam shaping and optimization based on a single aspheric lens. *Optics & Laser Technology* **183**, 112391 (2025).
19. García, R. Phase imaging atomic force microscopy. *Amplitude Modulation Atomic Force Microscopy*, 91-101 (2010).
20. Oh, H.M. et al. Photochemical Reaction in Monolayer MoS_2 via Correlated Photoluminescence, Raman Spectroscopy, and Atomic Force Microscopy. *ACS Nano* **10**, 5230-5236 (2016).
21. Wu, Q. et al. Space-Confined One-Step Growth of 2D MoO_2/MoS_2 Vertical Heterostructures for Superior Hydrogen Evolution in Alkaline Electrolytes. *Small* **18**, 2201051 (2022).